Experimental demonstration of indoor interfered visible light communication system employing successive interference cancellation

Miaofeng Li (李淼峰)[1,2], Xiang Li (李 响)[2,*], Chao Yang (杨 超)[2],
Qi Yang (杨 奇)[2], and Shaohua Yu (余少华)[1,2]

[1]*Wuhan National Laboratory for Optoelectronics, Huazhong University of Science and Technology,
Wuhan 430074, China*
[2]*State Key Laboratory of Optical Communication Technologies and Networks, Wuhan Research
Institute of Posts Telecommunications, Wuhan 430074, China*
Corresponding author: lixiang@wri.com.cn

Multipath interference induced power fading occurs when the transmission path lengths from the light emitting diodes to a single receiver are different in a visible light communication system. To solve this problem, we apply a QR-decomposition-based channel equalizer (QR-CE) to achieve successive interference cancellation for a discrete Fourier transform spreading (DFT-S) orthogonal frequency division multiplexing (OFDM) signal. We experimentally demonstrate a 200 Mb/s DFT-S OFDM over a 2 m free-space transmission. The experimental results show that a DFT-S OFDM with QR-CE attains much better bit error rate performance than a DFT-S OFDM with conventional CEs. The impacts of several parameters on a QR-CE are also investigated.

OCIS codes: 060.2605, 200.2605, 230.3670.
doi: 10.3788/COL201715.050604.

White light emitting diodes (LEDs) have been regarded as a promising technology for future illumination infrastructure. Compared with the traditional fluorescence of incandescent lamps, LEDs can provide high efficiency, low voltage and current requirements, long lifetime, and high reliability[1]. Nowadays, LEDs have been widely used in flat panel displays, illumination, and various indicator applications. In recent years, simultaneous illumination and visible light communication (VLC) based on LEDs have attracted a lot of attention in the next generation indoor wireless local area networks due to the advantages of long lifetime, low cost, small size, unlicensed spectrum, high security, and immunity to electromagnetic interference[2–6]. However, the intrinsic modulation bandwidth of a commercially available phosphor-coated white LED is limited to several tens of megahertz (MHz) due to its high diffusion capacitance and resistance for illumination[6]. Therefore, a high spectral efficiency modulation format such as orthogonal frequency division multiplexing (OFDM) or its baseband form, discrete multi-tone (DMT), has been proposed to increase the capacity under such limited bandwidth[7,8].

It is also proved that the arrangement of the relative locations of transmitters and receivers has great influences on the performances of indoor VLC systems. In a practical indoor environment, multiple LEDs are required to be placed properly to realize full-range illumination and optical wireless communication with similar performances. The optical multipath effects induced by multiple LEDs have been investigated[9,10]. It has been shown that the differences in optical path lengths among different LEDs

only have slight effects on the overall performance. As shown in Fig. 1, multiple LEDs may have similar contributions to the overlapped area due to similar optical path lengths. It is noted that if the optical path lengths are quite different among the LEDs, the optical powers at the overlapped area are also quite different, resulting in trivial delay interference. However, multipath delays caused by different lengths of electrical transmission lines of LEDs have been studied recently, where the overlapped area may receive the signal with similar power but different delays from multiple LEDs[11,12].

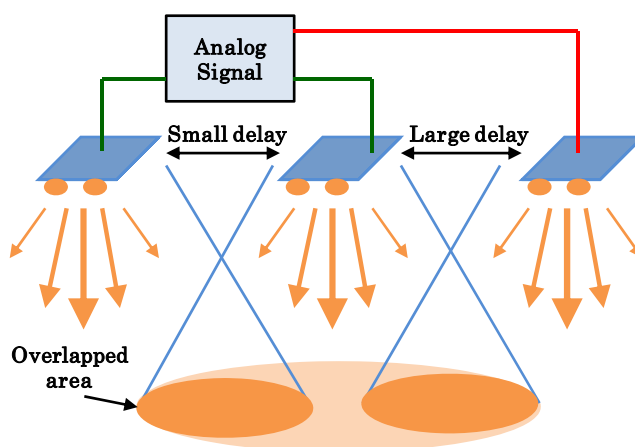As shown in Fig. 1, the relative delay between adjacent LEDs may cause severe power fading at the overlapped

Fig. 1. Practical scheme utilizing multiple LEDs to achieve full-range illumination and VLC.

area. Therefore, interference mitigation schemes are required in the practical indoor VLC systems. To overcome the delay interference, Alamouti space-time block coding (STBC), which has been proposed in several wireless communication standards[13], is also applied to resist the multipath effect in the VLC system[11,12]. However, the performance of Alamouti STBC is worse than conventional repetition coding under the small relative delay condition due to the smaller received signal power and low signal-to-noise ratio (SNR). In addition, unlike the repetition coding scheme, STBC may require additional digital-to-analog converters (DACs) at the transmitter side to modulate different coded signals to different LEDs, which may increase the cost and complexity of the system.

Our previous work in Ref. [14] has shown that the successive interference cancellation (SIC) technique can be used to combat power fading induced by polarization mode dispersion in a direct-detection zero-padding OFDM (ZP-OFDM) system. In this Letter, we apply the SIC technique to mitigate the multipath effects in multiple LED transmission systems. We apply a QR-decomposition-based channel equalizer (QR-CE) in discrete Fourier transform spreading (DFT-S) OFDM to deal with the power fading in the overlapped areas and achieve SIC. It is noted that the data information in OFDM subcarriers are correlated due to the DFT spreading, which can be seen as a "known interference." We experimentally demonstrate DFT-S OFDM optical wireless transmission with 2 m distance in a two LEDs transmission system at a raw rate of ~200 Mb/s occupying a 50 MHz bandwidth with different relative delays and transmitting power. The experimental results show that the bit error rate (BER) performance of the QR-CE is better than that of a conventional CE (CCE) in DFT-S OFDM and OFDM-based VLC systems with multipath interference between two LEDs. Further study shows that DFT-S OFDM with four sub-bands and one pilot in each OFDM symbol can balance the performance and spectral efficiency. It is also shown that schemes of sub-band mapping have no effect on the overall performance.

In a DFT-S OFDM transmitter, one OFDM symbol, represented as $MV \times 1$ payload vector $\mathbf{S}_{MV}$, is partitioned into V sub-bands with M subcarriers each. It is noted that interleaved and localized schemes are two popular sub-band partition methods for DFT-S OFDM, as shown in Fig. 2. We denote the $M \times 1$ vector $\mathbf{S}_M^V$ as the vth signal sub-band. DFT spreading is achieved by pre-coding the $M \times M$ DFT matrix $\mathbf{F}_M$ on each sub-band. After DFT spreading, the payload information in the subcarriers is correlated, which can be viewed as "known inter-carrier interference (ICI)." Another $N \times N$ $(N > MV)$ inverse DFT (IDFT) matrix $\mathbf{F}_N^{\mathbf{H}}$ is then applied to transform the signal from the frequency domain to the time domain. At the receiver side, after removing the cyclic prefix (CP), the DFT matrix $\mathbf{F}_M$ is applied to the received time-domain samples. For easy analysis, we only consider the M payload subcarriers in one sub-band in one OFDM symbol. The received $M \times 1$ signal vector $\mathbf{Y}_M^V$ in the frequency domain in the vth sub-band can be expressed as
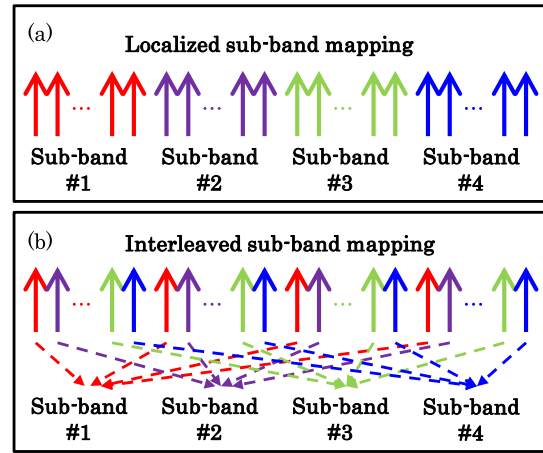

Fig. 2. Sub-band mapping with (a) localized and (b) interleaved schemes.

$$\mathbf{Y}_M^V = \mathbf{D}_M(\mathbf{h}_M^V)\mathbf{F}_M\mathbf{S}_M^V, \tag{1}$$

where $\mathbf{h}_M^V$ is an $M \times 1$ vector representing the channel frequency response for the payload subcarrier of the vth sub-band; $\mathbf{D}_M(\mathbf{h}_M^V)$ denotes an $M \times M$ diagonal matrix with $\mathbf{h}_M^V$ on its diagonal. We then define the $M \times M$ matrix $\mathbf{G}_M = \mathbf{D}_M(\mathbf{h}_M^V)\mathbf{F}_M$ and apply QR decomposition to $\mathbf{G}_M$ based on the modified Gram–Schmidt algorithm[15]. Thus, Eq. (1) can be rewritten as

$$\mathbf{Y}_M^V = \mathbf{G}_M\mathbf{S}_M^V = \mathbf{Q}_M\mathbf{R}_M\mathbf{S}_M^V, \tag{2}$$

where $\mathbf{Q}_M$ is an $M \times M$ matrix with orthogonal columns, and $\mathbf{Q}_M\mathbf{Q}_M^{\mathrm{H}}$ is an identity matrix; $\mathbf{R}_M$ is an $M \times M$ upper triangular matrix. By multiplying $\mathbf{Y}_M^V$ with $\mathbf{Q}_M^{\mathrm{H}}$, then Eq. (2) can be rewritten as

$$\tilde{\mathbf{Y}}_M^V = \mathbf{Q}_M^{\mathrm{H}}\mathbf{Y}_M^V = \mathbf{Q}_M^{\mathrm{H}}\mathbf{Q}_M\mathbf{R}_M\mathbf{S}_M^V = \mathbf{R}_M\mathbf{S}_M^V, \tag{3}$$

Due to the upper triangular structure of $\mathbf{R}_M$, the ith element of $\tilde{\mathbf{Y}}_M^V$ is given by

$$\tilde{\mathrm{Y}}_M^V(i) = \mathrm{R}_M^{i,i}\mathrm{S}_M^V(i) + \sum_{k=i+1}^{M} \mathrm{R}_M^{i,k}\mathrm{S}_M^V(k), \tag{4}$$

where $\mathrm{R}_M^{i,k}$ is the (i,k)th element of matrix $\mathbf{R}_M$, and $\mathrm{S}_M^V(i)$ is the ith element of vector $\mathbf{S}_M^V$. From Eq. (4), we can see that $\tilde{\mathrm{Y}}_M^V(i)$ is free of interference from the payload information from subcarrier indexes 1 to $i-1$. Therefore, the payload in the ith subcarrier of vth sub-band $\mathrm{S}_M^V(i)$ can be recovered via the corresponding data in subcarrier indexes $i+1$ to M iteratively, which is given by

$$\mathrm{S}_M^V(i) = \frac{\tilde{\mathrm{Y}}_M^V(i) - \sum_{k=i+1}^{M} \mathrm{R}_M^{i,k}\langle\mathrm{S}_M^V(k)\rangle}{\mathrm{R}_M^{i,i}}, \tag{5}$$

where $\langle\mathrm{S}_M^V(k)\rangle$ is the decision of payload information at the kth subcarrier of the vth sub-band $\mathbf{S}_M^V$ [e.g. $\pm 1 \pm j$ for quadrature phase-shift keying (QPSK) modulation].

From Eq. (5), we can see that the accuracy of $\langle S_M^V(k) \rangle$ is actually dependent on the decision of the payload information from subcarriers $i+1$ to M. Therefore, we can choose several pilot subcarriers, e.g. $S_M^V(M)$, $S_M^V(M-1)$, to increase the decision accuracy at the initial iteration stage. In this Letter, the CCE reported in Refs. [16,17] for DFT-S OFDM is chosen for performance comparison with the QR-CE. The digital signal processing (DSP) schemes of the DFT-S OFDM with QR-CE and CCE at the receiver side are shown in Fig. 3. From Fig. 3, we can see that the steps, including CP removal, fast Fourier transform (FFT) demodulation, and training symbol (TS)-based channel estimation, are the same for both of the CEs. For the DFT-S OFDM signal with CCE, due to the DFT pre-coding for each sub-band at the transmitter side, inverse FFT (IFFT) is required at the receiving side to demodulate the signal for each sub-band before channel compensation, as shown in Fig. 3(a). For the DFT-S OFDM signal with QR-CE, from the derivations of Eqs. (1) to (5), we can recover the original signal $\mathbf{S}_M^V$ in each sub-band sequentially once the value of $\mathbf{h}_M^V$ is obtained after channel estimation, as shown in Fig. 3(b). It is noted that in our previous scheme for ZP-OFDM, the QR decomposition and iterative signal equalization are performed for the entire OFDM band. However, the matrix or vector size is much smaller after the sub-band partition. Therefore, the computational complexity is reduced significantly.

Figure 4 shows the experimental setup, similar to Refs. [12,13], employing two LEDs to emulate an indoor VLC system with the air transmission distance of 2 m. The delay interference is introduced by the lengths between two electrical transmission lines, which can be adjusted between 0 to 3 m. The normal OFDM and DFT-S OFDM signals are generated off-line and then loaded into an arbitrary waveform generator (AWG, Tektronix 7122 C, bandwidth up to 5.3 GHz, 10 bit resolution) operating at 200 MS/s. Two commercial available phosphor-coated

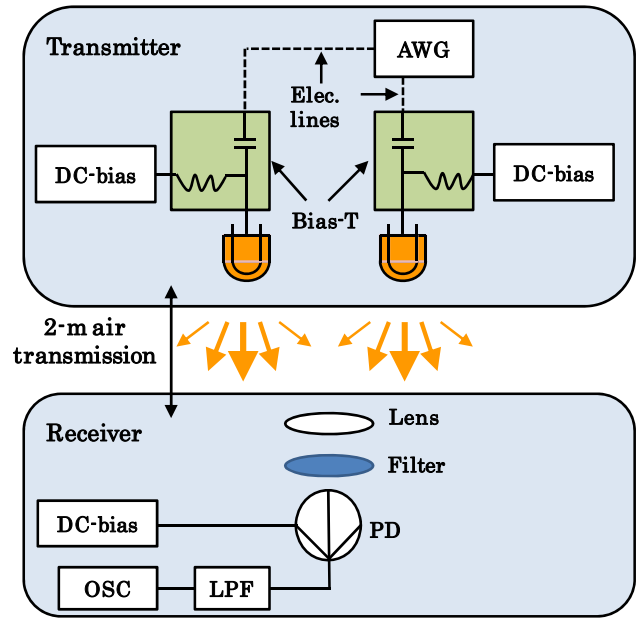Fig. 3. DSP schemes at the receiver side for (a) CCE and (b) QR-CE.

Fig. 4. Experimental setup of the 2 m free-space VLC system with delay-line interference. OSC: oscilloscope; LPF: low-pass filter[11,12].

white LEDs (Cree R5) are used as the transmitters, which can generate a luminous flux of 139 lm at driving currents of 350 mA. The two outputs of the AWG are connected to the electrical lines with an adjustable length and then fed onto the two LEDs by two bias-Ts. It is noted that the generated signals at the two output ports of the AWG contain the same information with an adjustable electrical power. After the 2 m free-space transmission, an optical band-pass filter with a cut-off wavelength of 500 nm is applied to remove the phosphorescent component of the LED radiation. A plano-convex glass lens is also used to focus the light onto the active area of the photodetector (PD). The PD (Hamamatsu S6968) has a cut-off frequency of 50 MHz at 850 nm and active area of 150 mm^2. After optical-to-electrical conversion, the signal is first calibrated via an RC equalization circuit, and then sampled by a Tektronix oscillator scope of DPO73304D operating at 1 GSa/s for off-line processing.

In our experiment, the DFT size is 512 with 128 subcarriers occupying a 50 MHz bandwidth that are filled with data to achieve a real-valued signal with Hermitian symmetry. Both interleaved and localized sub-band mapping schemes, as shown in Fig. 2, are considered in the experiment for DFT-S OFDM. For each OFDM symbol, four sub-bands with one pilot subcarrier in each sub-band are used for the initial iteration in the QR-CE. All of the subcarriers are modulated with a 16 quadrature amplitude modulation (QAM) format. The length of the CP is eight. Ten TSs are used for channel estimation followed by 300 OFDM payload symbols. Therefore, the net data rate is 178.1 Mb/s after excluding the 7% forward error correction (FEC) overhead. Power loading for the two LEDs is performed independently before the payload
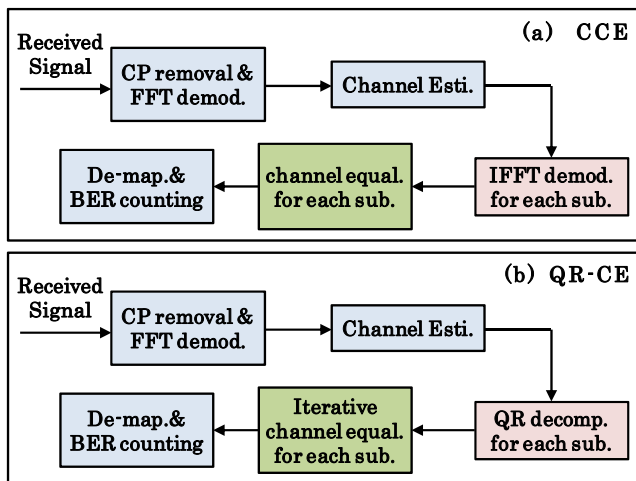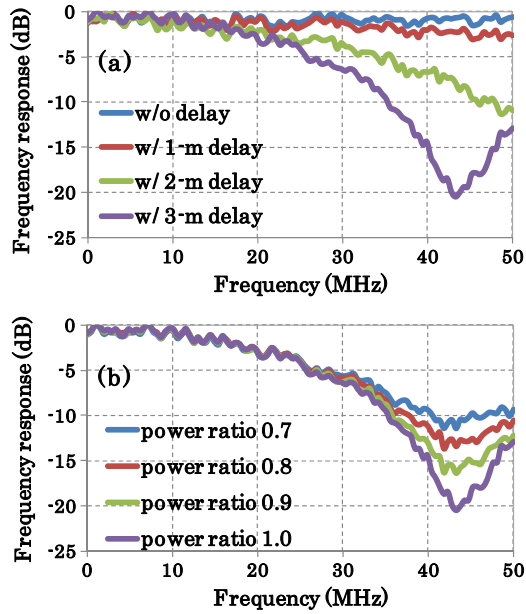
Fig. 5. Measured channel response of the signal under various (a) relative delays with power ratio of one and (b) power ratios with a relative delay of 3 m.
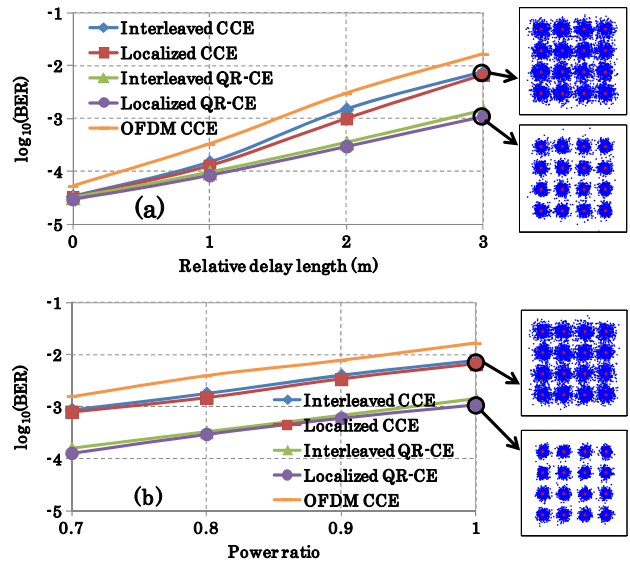

Fig. 6. BER performances of the DFT-S OFDM signal with QR-CE and CCE, and a normal OFDM versus (a) relative delays at power ratio of one and (b) power ratios at a relative delay of 3 m under different sub-band mapping schemes.

signal transmission. Therefore, the power fading due to the limited bandwidth of the LEDs can be ignored.

Figures 5(a) and 5(b) show the measured channel frequency response of the signal at different relative delays and power ratios. As shown in Fig. 5(a), compared with the delay-line interference free case, the received signals suffer from power fading which is induced by the delay-line interference at the frequency of the half-reciprocal of the relative delay time. When the relative delay length is smaller, the channel is less affected by the delay interference with shallower notches. The channel frequency response is also influenced by the difference of the received power from two LEDs. As can be seen from Fig. 5(b), the power fading is more severe when the electrical power to the two LEDs is closer.

Figures 6(a) and 6(b) show the BER performances under different relative delay lengths and power ratios for the QR-CE and CCE with different sub-band mapping schemes. From Fig. 6, we can see that the performances of the QR-CE and CCE are both degraded with an increased relative delay length and power ratio. However, the QR-CE provides better BER performance than the CCE under worse channel conditions and can achieve 7% FEC threshold (BER = 3.8×10^{-3}) in the experiment demonstration. It is also shown that the sub-band mapping scheme has no significant effect on the overall performances for both the QR-CE and CCE. The corresponding constellations are also shown in the insets of Figs. 6(a) and 6(b), respectively. For a fair comparison, the performance of a normal OFDM is also included in Fig. 6. Due to a higher peak-to-average power ratio (PAPR), the performance of the OFDM is worse than the DFT-S OFDM, which agrees well with previous results in an optical fiber transmission system.

The performance improvement of the QR-CE mainly comes from the "known interference" introduced in the OFDM symbol by DFT-S, which can be used to recover the signal in a specific subcarrier that is severely undermined due to power fading. For the CCE, the payload information in each subcarrier is recovered independently. However, for the QR-CE, the signal in each subcarrier is recovered one-by-one. The accuracy of the signal in the current recovered subcarrier is dependent on the accuracy of the previously recovered subcarrier signal, where the "known ICI" is canceled successively. It is noted that the "known ICI" is introduced by DFT-S at the transmitter side. Therefore, signals in the subcarriers are correlated with each other. It is because of the "known ICI" that the DFT-S OFDM signals can be recovered sequentially, while a normal OFDM signal cannot.

In Figs. 7(a) and 7(b), we study the effects of the number of sub-bands and pilots on the BER performance of the QR-CE under the environment of a power ratio of one, respectively. The scheme of interleaved sub-band mapping is considered. It is shown in Fig. 7(a) that the BER performance is best when the number of sub-bands is four. It can be explained as the sequence length for the QR-CE is smaller at a larger number of sub-bands, which leads to a more accurate QR decomposition and a lower possibility of error occuring during the sequence detection process. However, a larger number of sub-bands may result in a higher PAPR, where the overall performances may be undermined due to the nonlinear characteristics of the LED, as shown in Fig. 8. In addition, although a smaller number of sub-bands has a lower PAPR, it may result in a higher computational complexity due to the larger size of $\mathbf{S}_M^V$ in Eq. (1). In the QR-CE, pilots are required for the initial channel equalization in each sub-band. A larger
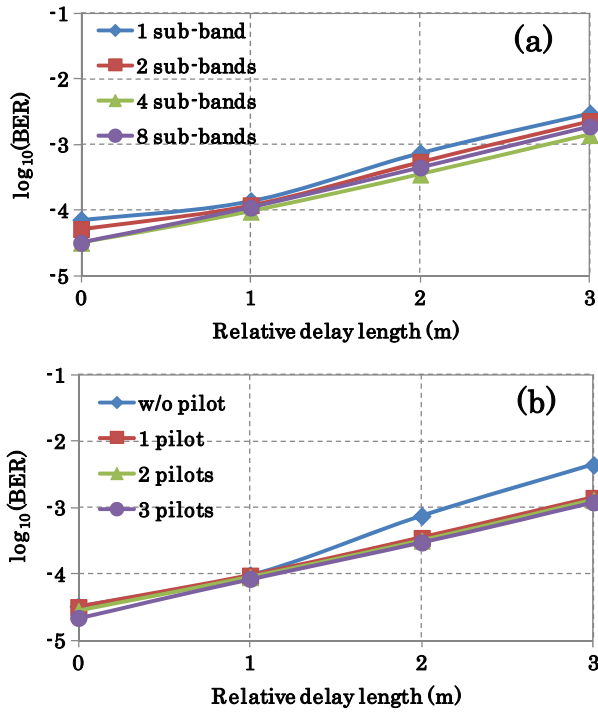
Fig. 7. BER performances of the QR-CE with (a) a different number of sub-bands and (b) a different number of pilots for the QR-CE.
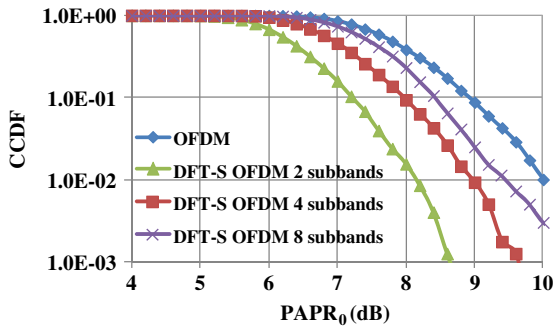

Fig. 8. Complementary cumulative distribution function (CCDF) versus PAPR for a normal and DFT-S OFDM with a different number of sub-bands, respectively.

number of sub-bands and pilots indicate a lower spectral efficiency. As shown in Fig. 7(b), aone pilot in each sub-band (four sub-bands) is sufficient for the QR-CE to achieve the optimum performance and maintain a high spectral efficiency.

In this Letter, we experimentally investigate the effects of the delay-line interference between two LEDs in an indoor VLC system with 2 m free-space transmission distance. The signal suffers more from the delay-line interference when the relative delay is large and the power ratio is close to 1. DFT-S OFDM combined with QR-CE is proposed to combat the power fading effects induced by the delay-line interference. The experimental results show that DFT-S OFDM with QR-CE performs better than CCE, which can achieve the BER of 3.8×10^{-3} over a 2 m free-space transmission with a 3 m delay-line difference. The performance improvement mainly comes from the "known ICI" introduced by DFT-S followed by SIC in the QR-CE. It is also shown that four sub-bands with one pilot in each sub-band are sufficient for achieving the optimal performance and maintaining the high spectral efficiency. The sub-band mapping scheme of the DFT-S OFDM has no significant effects on the overall transmission performance. For the QR-CE, the QR decomposition is performed on the square matrix and only related to the channel state information that can be computed before the signal transmission. Therefore, the DFT-S OFDM with QR-CE offers a cost effective solution to overcome the multipath interference problem among LEDs in indoor VLC systems.

References

1. C. L. Liao, Y. F. Chang, C. L. Ho, and M. C. Wu, IEEE Electron. Device Lett. **34**, 611 (2013).
2. J. Luo, Y. Tang, H. Jia, Q. Zhu, and W. Xue, Chin. Opt. Lett. **14**, 120604 (2016).
3. Y. Wu, A. Yang, L. Feng, and Y. Sun, Chin. Opt. Lett. **11**, 030601 (2013).
4. J. Ding, Z. Huang, and Y. Ji, Chin. Opt. Lett. **8**, 1182 (2010).
5. Z. Huang and Y. Ji, Chin. Opt. Lett. **10**, 050602 (2012).
6. J. Zhao, C. Qin, M. Zhang, and N. Chi, Photon. Res. **4**, 249 (2016).
7. Y. Wang, Y. Wang, and N. Chi, Photon. Res. **2**, 138 (2014).
8. X. Huang, S. Chen, Z. Wang, Y. Wang, and N. Chi, Chin. Opt. Lett. **13**, 100602 (2015).
9. T.-H. Do, J. Hwang, and M. Yoo, Photon. Netw. Commun. **25**, 60 (2013).
10. Z. Wang, C. Yu, W.-D. Zhong, J. Chen, and W. Chen, Opt. Express **20**, 4564 (2012).
11. C.-C. Wei, F.-M. Wu, Z.-Y. Chen, C.-T. Lin, Y.-J. Chen, and S. Chi, in *Optical Fiber Communication Conference* (2014), paper Th1F.3.
12. C.-C. Wei, F.-M. Wu, Z.-Y. Chen, C.-T. Lin, Y.-S. Huang, Y.-J. Chen, and S. Chi, J. Opt. Commun. Netw. **7**, A459 (2015).
13. V. Tarokh, H. Jafarkhani, and A. R. Calderbank, IEEE J. Sel. Areas Commun. **17**, 451 (1999).
14. X. Li, A. Alphones, W. D. Zhong, and C. Yu, Opt. Express **21**, 20851 (2013).
15. Z. Huang and P. Tsai, IEEE Trans. Circuits Syst. I, Reg. Pap. **58**, 2531 (2011).
16. Z. Huang, F. Zhang, and Z. Chen, Chin. Opt. Lett. **11**, 060601 (2013).
17. R. Ding, T. Zhang, and F. Zhang, Chin. Opt. Lett. **12**, 110604 (2014).